Cold Pool Dynamics Shape the Response of Extreme Rainfall Events to Climate Change

Lochbihler, Kai; Lenderink, Geert; Siebesma, A. Pier

DOI
10.1029/2020MS002306

Publication date
2021

Document Version
Final published version

Published in
Journal of Advances in Modeling Earth Systems

Citation (APA)
Lochbihler, K., Lenderink, G., & Siebesma, A. P. (2021). Cold Pool Dynamics Shape the Response of Extreme Rainfall Events to Climate Change. *Journal of Advances in Modeling Earth Systems*, *13*(2), 1-16. Article e2020MS002306. https://doi.org/10.1029/2020MS002306

JAMES | Journal of Advances in Modeling Earth Systems

RESEARCH ARTICLE
10.1029/2020MS002306

Cold Pool Dynamics Shape the Response of Extreme Rainfall Events to Climate Change

Kai Lochbihler[1,2], **Geert Lenderink**[1], **and A. Pier Siebesma**[1,2]

[1]The Royal Netherlands Meteorological Institute (KNMI), De Bilt, The Netherlands, [2]Delft University of Technology, Delft, The Netherlands

Key Points:

- Warmer conditions lead to more intense and larger rain cells
- Rain cell properties show distinct, well-defined relations with cold pool properties
- Largest variations at high temperature, with reductions of RH leading to very strong cold pool dynamics and vigorous rain systems

Supporting Information:

- Supporting Information S1

Correspondence to:
K. Lochbihler,
lochbihl@knmi.nl

Citation:
Lochbihler, K., Lenderink, G., & Siebesma, A. P. (2021). Cold pool dynamics shape the response of extreme rainfall events to climate change. *Journal of Advances in Modeling Earth Systems*, *13*, e2020MS002306. https://doi.org/10.1029/2020MS002306

Received 21 AUG 2020
Accepted 17 DEC 2020

Abstract There is increasing evidence that local rainfall extremes can increase with warming at a higher rate than expected from the Clausius-Clapeyron (CC) relation. The exact mechanisms behind this super-CC scaling phenomenon are still unsolved. Recent studies highlight invigorated local dynamics as a contributor to enhanced precipitation rates with warming. Here, cold pools play an important role in the process of organization and deepening of convective clouds. Another known effect of cold pools is the amplification of low-level moisture variability. Yet, how these processes respond to climatic warming and how they relate to enhanced precipitation rates remains largely unanswered. Unlike other studies which use rather simple approaches mimicking climate change, we present a much more comprehensive set of experiments using a high-resolution large eddy simulation (LES) model. We use an idealized but realistically forced case setup, representative for conditions with extreme summer precipitation in midlatitudes. Based on that, we examine how a warmer atmosphere under the assumption of constant and varying relative humidity, lapse rate changes and enhanced large-scale dynamics influence precipitation rates, cold pool dynamics, and the low-level moisture field. Warmer conditions generally lead to larger and more intense events, accompanied by enhanced cold pool dynamics and a concurring moisture accumulation in confined regions. The latter are known as preferred locations for new convective events. Our results show that cold pool dynamics play an increasingly important role in shaping the response of local precipitation extremes to global warming, providing a potential mechanism for super-CC behavior as subject for future research.

Plain Language Summary Observations and models show that rain extremes are increasing with global warming. Aggregated over large areas and long-time intervals, this increase will roughly follow the higher water holding capacity of air at a warmer temperature. However, local extreme storms show a much stronger response. This indicates that, in addition to a potentially greater local moisture availability in a warmer climate, rain events consume moisture from a larger area. Investigating this aspect requires expensive high-resolution models. We do this by simulating a typical summer day with heavy rainfall on an area roughly the size of the Netherlands. By changing the temperature along with other characteristics of the atmosphere, we mimic the impact of climatic change. Our results show that warmer conditions generally lead to larger and more intense storms. Furthermore, we find that moisture transport near the surface through the winds created by storms plays an important role. This can result in an accumulation of moisture at certain locations that stems from greater distances away. Freshly developing storms eventually can harvest this additional moisture. This feedback process intensifies under warmer and moister conditions and provides a potential mechanism for the strong increase of local rainfall extremes in a warmer climate.

1. Introduction

Precipitation extremes are commonly expected to increase with global temperature rise. Global climate model simulations show, that on large spatial and long temporal scales, the Clausius-Clapeyron (CC) relation presents a robust constraint in this context (Pall et al., 2007; Tebaldi et al., 2006). However, there are indications that on small spatial and short temporal scales a warming atmosphere enables rainfall amounts to increase above the CC rate of 7 % $°C^{-1}$. For instance, Lenderink and van Meijgaard (2008) and Loriaux et al. (2013) showed that extremes of hourly and subhourly precipitation observations in the Netherlands exhibit an increase with warming up to 14 % $°C^{-1}$. Similar results have been obtained for other locations, for

example, in Germany (Berg et al., 2013; Moseley et al., 2013), Hong Kong (Lenderink et al., 2011), and some regions of Australia (Wasko et al., 2018).

The mechanism behind the phenomenon of enhanced precipitation scaling with warming beyond the CC rate is still subject to ongoing research. A common theory suggests that invigorated convective updrafts through additional latent heating amplify moisture convergence and therefore moisture supply to the storm itself (Trenberth et al., 2003). Indeed, enhanced large-scale convergence is often found in combination with high precipitation rates and even further increases at warmer and moister surface conditions (Lenderink et al., 2017). The spatial properties of rainfall events might also play a crucial role here. Rain radar data analysis reveals that convective rain cells grow larger and intensify over most of their area at higher temperatures and moisture availability (Lochbihler et al., 2017). Similar results from LES simulations confirm that size and intensity of rainfall events are clearly linked in such a scenario (Lochbihler et al., 2019). This indicates that enhanced precipitation intensities are at least partly attributable to a larger area of moisture supply to the storm.

Another potential driver for enhanced precipitation rates with warming is cloud-cloud interaction through cold pools. According to Tompkins (2001), cold pools generally evolve in the following manner. After an initial cooling and moistening of the subcloud layer through the evaporation of falling rain drops, the resulting relatively cold and dry air masses descend to lower levels, driven by gravity, and eventually reach the surface. This forces the cold pool to spread horizontally and while it remains relatively dry in the center the edges are moist. The resulting dynamics let cold pools play an important role for the formation of deep convection. If cold pool formation is suppressed, clouds remain small and shallow (Böing et al., 2012; Khairoutdinov & Randall, 2006). Furthermore, the triggering of convection at cold pool edges (e.g., Hirt et al., 2020; Seifert & Heus, 2013; Tompkins, 2001; Torri et al., 2015) or by collision of two or more cold pools (e.g., Haerter et al., 2019) plays a crucial role in the process of convective self-aggregation and organization.

Cold pool dynamics also modify the local low-level moisture field and, hence, moisture availability to convective clouds. For instance, Schlemmer and Hohenegger (2016) show, by using idealized Large eddy simulations (LES), that most of the accumulated moisture in nonprecipitating regions stems from the advection through laterally spreading cold pools. Other sources, for example, surface fluxes, play a rather minor role in this context (Fuglestvedt & Haerter, 2020; Schlemmer & Hohenegger, 2016). These regions of relatively higher moisture content are then preferred locations for new convective cells. Evidence for the link between cold pool induced moisture convergence and subsequent convective events is further strengthened by Fuglestvedt and Haerter (2020). The authors use a back tracking method to establish a direct connection between cold pools as moisture conveyors and new convective rain events.

In this study, we use an LES model (200 m resolution on a 192 × 192 km domain) to analyze cold pool properties, and their relation to rainfall rates, for a case of heavy convection at midlatitudes. Previous studies have used rather simple perturbations to mimic climate change (e.g., Haerter & Schlemmer, 2018), but here we present a much larger set of perturbed experiments. These perturbations reflect warmer climatic perturbations, and cooler as well, based on projected changes of large-scale conditions in global climate model simulations. As such, besides perturbations with uniform vertical warming, and constant relative humidity, also different perturbations with enhanced warming at upper levels (reflecting a stabilization of the atmosphere in terms of the dry lapse rate) and decreased relative humidity are studied. Although these perturbations cover a broad range of possible future conditions, they obviously do not sample climate change to a full extent.

These experiments also differ from the radiative-convective equilibrium (RCE) simulations performed for the tropics where CC-scaling robustly applies (e.g., Fildier et al., 2017; Romps, 2011). Instead of studying the quasiequilibrium response in RCE, we use a strongly time varying forcing which destabilizes the atmosphere and provides moisture, and which are connected to surface fluxes and the passage of a larger-scale (synoptic) disturbance. For each of the resulting 25 experiments, we identify rain events, cold pools, and moist areas by a clustering method. We investigate how the intensity and size of rain events differs between the different simulations and how cold pool activity and the low-level moisture field relates to that.

2. Methods

2.1. Simulation Setup

We use the Dutch Atmospheric Large Eddy Simulation (DALES) model (version 4.1; Böing et al., 2012; Heus et al., 2010) with a single moment cloud microphysics scheme (Böing et al., 2012; Grabowski, 1998). The evaporation of rain drops is parameterized as a function of the saturation deficit of the surrounding air mass, making the model suitable to study the effects of cold pools. The large-scale forcings, radiative cooling (1.5 K/day) and surface fluxes are prescribed. The simulations run with a horizontal resolution of 200 m on a domain of 192 × 192 km. The vertical grid has 240 levels with a variable layer thickness ranging from 40 m near the surface to 150 m at the top.

The case setup and forcing is similar to the LES simulation in Lochbihler et al. (2019) and Loriaux et al. (2017). They were derived from a typical summer day with extreme precipitation in the Netherlands under current climate providing initial conditions (Figure 1), surface forcing and large-scale winds, including the large-scale vertical velocity, omega (see Lochbihler et al., 2019 for details). In contrast to the case setup in Lochbihler et al. (2019), we used a normal day length, but to allow a longer period of organized convection, we instead extended the peak forcing of omega and surface fluxes during the second half of the simulation (see Figures S1 and S2). This is primarily needed to provide more robust statistics and to overcome limitations from the initialization by spatially uniform conditions leading to an initial convective state which is still characterized by many (unorganized) small-scale showers and considered less realistic (see also Lochbihler et al., 2019). After this initial state, the precipitation field transforms into fewer but larger multicell events. We refer to this characteristic when we use the term organized.

In addition to the CTL run, we ran a large number of experiments with different perturbation strategies. In total, there are five groups of perturbations which are summarized in Table 1.

The first experimental group, named the TEMP group, perturbs the initial temperature profile in steps of 2 K from −4 K to +4 K with respect to CTL. This perturbation is constant with height. The profile of specific humidity is adjusted to keep relative humidity identical to CTL. This leads to an increase/decrease of dew point temperature as indicated in the experiment name tag. The changes in near surface dew point are used as a tag in all other experiments. We note that the stability of the atmosphere with respect to moist processes decreases from colder to warmer runs in such a setting.

Since relative humidity is generally expected to decrease with a warming atmosphere over land (e.g., O'Gorman & Muller, 2010), the second group, RH, introduces changes of relative humidity. This is achieved by taking the profiles of the TEMP group and further increase temperature by 1 K for P2K and 2 K for P4K (P2Krh and P4Krh). In case of the M2K and M4K experiments, temperature is lowered by the respective value (M2Krh and M4Krh). This causes an approximately uniform decrease of relative humidity for the warmer runs (P2Krh and P4Krh), whereas in the colder experiments, humidity is closer to saturation. Figure 1b illustrates this for the M4Krh and P4Krh experiments. The M2Krh and P2Krh experiments are approximately half way in between. We note that by applying this procedure, the absolute humidity of the air—near surface as measured by the dew point temperature but also in a vertically integrated sense—is the same as in the TEMP group.

In a similar way, but restricted to levels below 3 km, the experiments in the RHL group have a lower (higher) relative humidity for the P4Krhl (M4Krhl) experiments. Figure 1c illustrates this perturbation. This approach represents a more realistic vertical profile of relative humidity changes with warming specifically in the case of extreme precipitation events (see Figure 1b in Attema et al., 2014). To avoid an abrupt jump of temperature and relative humidity, we linearly interpolate temperature between 3 and 2 km. Below 2 km, the profiles are identical to the M4Krh and P4Krh experiments. We note that, whereas in RH the atmospheric dry lapse rate (dry stability) is unchanged compared to the TEMP group, in this experiment changes in dry stability occur due to the enhanced boundary layer warming imposed.

Atmospheric warming due to a climate change is expected to vary with height, which is primarily related to convection which tends to keep the atmospheric lapse rate close to a moist adiabat with greater warming aloft (Bony et al., 2006; Tett et al., 1996). To account for these changes in the thermal stratification as the atmosphere warms, we apply a nonuniform temperature perturbation. Using a similar approach as in Loriaux

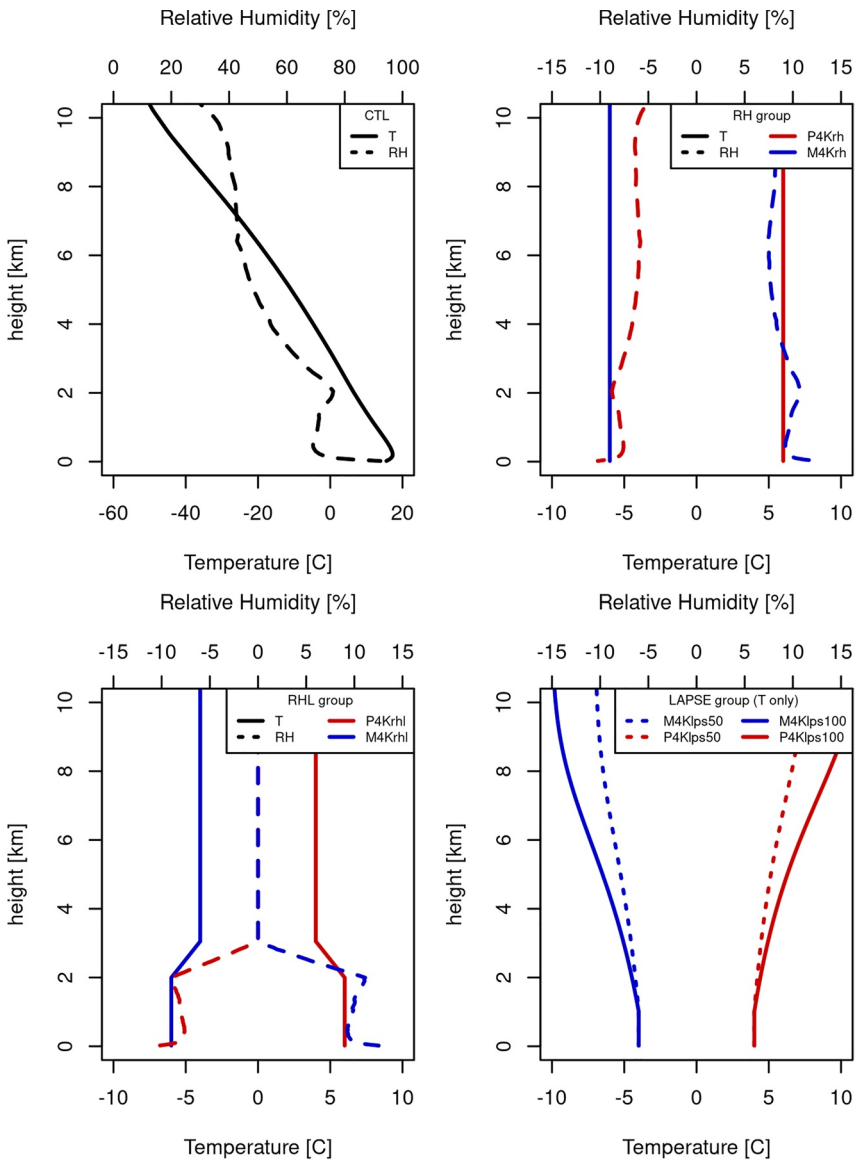

Figure 1. Initial temperature *T* and relative humidity RH profiles of the CTL setup (a) and the relative change of both variables for various types of perturbations, more specifically the RH (b), RHL (c), and LAPSE (d) groups. Note that, except for the LAPSE group, solid lines indicate temperature (bottom axis) and dashed lines represent relative humidity (top axis).

et al. (2013), the temperature perturbations of the experiments M4Klps100 and P4Klps100 of the LAPSE group follow a moist adiabatic lapse rate, while the M4Klps50 and P4Klps50 experiments are subjected to a temperature change that is halfway between a moist adiabatic perturbation and a uniform perturbation. More specifically, the resulting temperature profiles are a linear combination of a constant shift (e.g., P4K) and (the fraction of) a moist adiabatic temperature perturbation. For a more detailed description, see Section 5 in Loriaux et al. (2013). All profiles of the temperature perturbations from the LAPSE group are displayed in Figure 1d. Note, that all these perturbations are uniform below 1 km which is approximately equal to the height of the lifting condensation level. The specific humidity is modified in all the experiments of the LAPSE group to keep the relative humidity identical to CTL. Since moist adiabatic perturbations hardly affect the moist stability of the atmosphere, it should be noted that the destabilization of the atmosphere with warming is much stronger for the TEMP group than for the LAPSE group (see also Figure S3 that shows the time development of the CAPE of the various experiments). Also, we note that the vertically integrated

Table 1
Table of Experiments

Name tag	Group tag	Perturbation
• CTL	–	–
• M4K	TEMP	full-column −4K with const. RH
• M2K	TEMP	full-column −2K with const. RH
• P2K	TEMP	full-column +2K with const. RH
• P4K	TEMP	full-column +4K with const. RH
▲ M4Krh	RH	like M4K but with additional −2K; RH = CTL+10%
▲ M2Krh	RH	like M2K but with additional −1K; RH = CTL+5%
▲ P2Krh	RH	like P2K but with additional +1K; RH = CTL−5%
▲ P4Krh	RH	like P4K but with additional +2K; RH = CTL−10%
■ M4Krhl	RHL	like M4K but with additional −2K below 2 km
■ P4Krhl	RHL	like P4K but with additional +2K below 2 km
+ M4Klps50	LAPSE	M4K with 50% moist adiabat superimposed; RH = CTL
+ P4Klps50	LAPSE	P4K with 50% moist adiabat superimposed; RH = CTL
⊞ M4Klps100	LAPSE	M4K with full moist adiabat superimposed; RH = CTL
⊞ P4Klps100	LAPSE	P4K with full moist adiabat superimposed; RH = CTL
◇ CTLls30	LS	CTL with 30% enhanced large-scale convergence
⊕ CTLls60	LS	CTL with 60% enhanced large-scale convergence
◇ M4Kls30	LS	M4K with 30% enhanced large-scale convergence
◇ P4Kls30	LS	P4K with 30% enhanced large-scale convergence
⊕ M4Kls60	LS	M4K with 60% enhanced large-scale convergence
⊕ P4Kls60	LS	P4K with 60% enhanced large-scale convergence

Note. See text for a more elaborate explanation of the different perturbation strategies.

water vapor is not identical to the corresponding experiments in the TEMP group (compare Figure S4).

The last perturbation group varies the large-scale convergence (LS). Extreme precipitation events are often associated with a strong large-scale vertical lifting (Lenderink et al., 2017). Thus, we carry out an additional group of simulations, LS, with enhanced forcing of the large-scale vertical velocity, w_{ls}. This is done by increasing w_{ls} in the TEMP experiments by 30% and 60%.

As an aside we note that, due to intensive testing, we were able to obtain three realizations of the CTL and two of the M2K. They are represented as separate dots/lines in all following figures.

2.2. Identification of Rain Cells, Cold Pools, and Moist Patches

Following the approach of Lochbihler et al. (2017, 2019), we group continuous areas of surface precipitation to clusters hereby called rain cells. Two grid points belong to the same rain cell if they are neighbors in x or y direction. In order to avoid small cells with low intensity, grid points below a threshold of 0.6 mm h^{-1} are ignored. For the same reason we first coarse grain the precipitation output from a resolution of 200–400 m.

The principles of the described clustering process can also be used for the identification of cold pools. However, the detection criteria are obviously different. We follow the method of Schlemmer and Hohenegger (2014, 2016). Since a cold pool is a descending, relatively cold and dry air mass originating from evaporation of rain drops, the equivalent potential temperature (θ_e) is a suitable indicator to diagnose the presence of a cold pool. More specifically, we calculate a low-level average of θ_e and subtract the domain average for each time step to obtain the horizontal field anomaly $\Delta\theta_e$. Unlike Schlemmer and Hohenegger (2014, 2016), we have only output for two model levels at 20 m and 100 m. The $\Delta\theta_e$ fields are first coarse grained to the same resolution as the precipitation output and then smoothed with a Gaussian low-pass filter to remove remaining numerical noise. Figure 2a shows an example taken from the control simulation. In contrast to Schlemmer and Hohenegger (2014), we choose a less restrictive threshold for $\Delta\theta_e$ of −1 K. Testing has shown that this allows for smoother cold pool edges and thus reduces the cutoff of grid points which belong to the same cold pool. However, in accordance with Schlemmer and Hohenegger (2014), we neglect all cold pools that do not reach −2 K. In case of cold pools, we also aim to quantify the areal growth rate. Thus, information about overlapping cold pools from one time step to another are saved during the clustering procedure.

Finally, we also apply the clustering technique to field anomalies of water vapor specific humidity, Δq_v, to detect relatively moist areas in the domain, called moist patches (Schlemmer & Hohenegger, 2016). The same averaging and smoothing procedure is used as for $\Delta\theta_e$ is. The threshold for Δq_v is 0.75 g kg^{-1}.

2.3. Precipitation Measures, Characteristics of Rain Cells, Cold Pools, and Moist Patches

We use domain averaged precipitation statistics for a first basic comparison of the different perturbation groups. We apply the same threshold as used for the rain cell clustering procedure. Thus, grid points with a rain rate less than 0.6 mm h^{-1} are considered as zero precipitating. For each time step, we calculate the domain averaged conditional precipitation rate P_r and the precipitation area fraction α. P_r is the mean rainfall rate over all grid points with precipitation in the domain, hence the term conditional. Zero precipitating grid

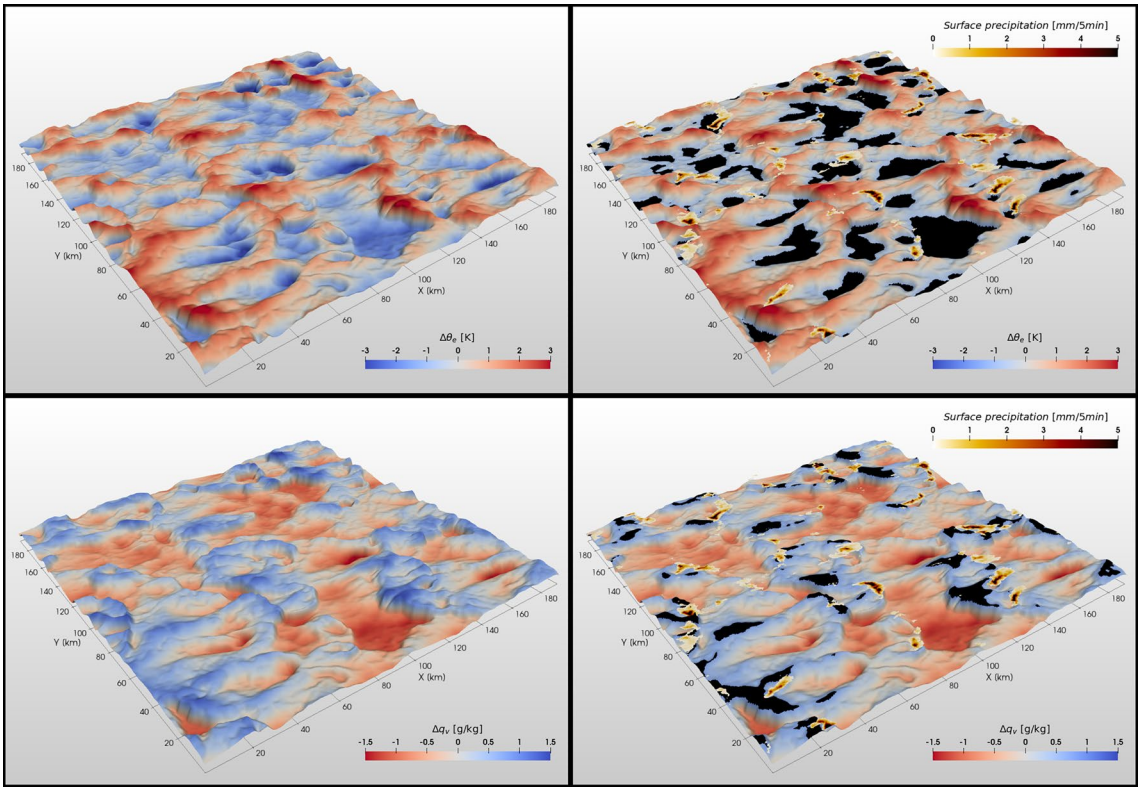

Figure 2. An illustration of the clustering of $\Delta\theta_e$ to cold pools (a and b) and Δq_v to moist patches (c and d). Left panels show the plain $\Delta\theta_e$ and Δq_v fields after 18 h simulation time. Identified cold pools and moist patches are overlaid in black in the right panels. Note that, in addition to the color mapping, the 2D fields are warped by the values of the respective variable for an easy visualization of the steep gradients along cold pool and moist patch edges. An animated video (video animation V1) showing the temporal evolution of the low-level $\Delta\theta_e$ fields is available from the supplementary material.

points are excluded from the averaging process. α is defined as the number of grid points with precipitation divided by the total number of grid points in the domain. In both cases, grid points with precipitation rates below the clustering threshold are considered as zero precipitating grid points.

The clustering algorithm allows the derivation of several metrics to describe the properties of rain cells, cold pools, and moist patches. The subscript i in the following definitions represents a single rain cell, cold pool, or moist patch. The linear size L_i of rain cell i is defined as the square root of the area A_i. Second, we calculate the average intensity of each cell $P_{i,r}$ by summing up the rain rates of all grid points belonging to a cell divided by their number. To capture the combined effect of rain cell area A_i and intensity $P_{i,r}$, we define $P_{i,\mathrm{car}}$ which is the product of the area and intensity and, thus, the total amount of rain produced by a rain cell per unit time.

In order to characterize cold pool activity, we make use of two measures. First, the cold pool volume $C_{i,v}$ which is defined as the product of the cold pool area and its average θ_e anomaly. This gives a combined estimate of how large and deep cold pools grow and, at the same time, allows for an easier visual interpretation than each variable separately. For the sake of an easier visual interpretation, we drop the negative sign of $C_{i,v}$. Second, we derive the areal growth rate of a cold pool $C_{i,\mathrm{gr}}$. This is done by matching overlapping cold pools in subsequent time steps and calculating the difference in area. Only cold pools that do not split in the next time step, and have not just merged, are considered (that is, only one forward link and zero or one back link in time). So area growth/decrease due to the merging or splitting of cold pools is excluded. To measure the growth of active cold pools, we restrict our analysis to those that grow in time and have an overlap with at least one rain cell.

The accumulation of low-level specific humidity in moist patches is measured in analogy to the cold pool volume. We therefore define the moist patch volume $M_{i,v}$ as the product of the moist patch area and its average Δq_v.

3. Results

3.1. Simulation Overview

The applied perturbation strategies create a diverse set of experiments. A modification of initial temperature, lapse rate, relative humidity, and large-scale convergence potentially influences several precipitation characteristics, for instance, the temporal evolution during the model day, rainfall intensities, and spatial properties of the precipitation field as well as individual events. In order to give an overview over the most fundamental differences between the experiment groups, we first focus on domain average precipitation statistics. Figure 3 shows the temporal evolution of the precipitation area fraction α and conditional rain rate P_r for the different groups.

The precipitation area fraction principally shows a similar temporal evolution for all experiments in all groups. Following an initial rapid increase after precipitation onset, the area fraction quickly decreases to a lower level for the rest of the simulation. In contrast to that, the rain rate rather continuously increases. This behavior has been described in Lochbihler et al. (2019) and essentially indicates a transition from a state with widespread small-scale unorganized showers to a state with a more limited number of showers, that are larger, more organized and more intense.

Besides these general commonalities of the experiments, there is a number of distinct differences between the groups. First and most obvious, the modification of relative humidity alters the timing of the precipitation onset. While the increased relative humidity in the M4Krh experiment shifts the precipitation onset toward the beginning of the simulation, we find a postponed onset in the P4Krh run. The other experiments line up in between at nearly constant intervals. This is most likely the effect of a lower lifting condensation level due to the higher relative humidity in the colder runs of the RH (and RHL) group. The opposite is the case in warmer simulations. Another difference between the TEMP and RH groups is a reversed order of the experiments with the highest area fraction during the first hours after precipitation onset. In the TEMP group, the P4K experiment shows the highest area fraction while in the RH group the M4Krh experiment sits on top. In a later stage of the simulation, these differences virtually vanish.

Compared to the TEMP group the warmer experiments in the RH group show larger temporal fluctuations, indicative of more vigorous dynamics. Additionally, within the RH group, the precipitation rates, after the onset of rain, spin up much faster in warmer experiments than in colder experiments and, in a similar way, temporal variability of the rain rate increases with warming. The large fluctuations of the area fraction and rain rate in the P4Krh experiment indicate short bursts of intense precipitation most likely caused by few but relatively large events; the smooth and steadily increasing rain rate in the M4Krh experiment on the other hand is symptomatic of numerous small, continuously emerging, and decaying events. According to Lochbihler et al. (2019), the enhanced temporal fluctuations in warmer runs can be traced back to a stronger stabilization of the atmosphere after precipitation rates peak. Subsequently, more time is needed until the prescribed large-scale convergence and surface fluxes refill the moisture deficit. The consequence is a more reduced rain activity after each burst of precipitation (see time series of CAPE and water vapor path in the Figures S3 and S4 in the supplement).

The temporal evolution of surface precipitation in the other groups follows very similar paths. In the same way as the RH group, the experiments in the RHL group show substantial shifts of the precipitation onset. The time difference is about 5 h. However, in contrast to the RH group the initial precipitation area fraction for the P4Krhl experiment is higher than in the M4Krhl run. Nevertheless, just as in the RH group, both the increase in rain rate over time and the temporal variability are lower in the colder than in the warmer runs.

With an increased large-scale convergence in the LS group, we observe a generally increased area fraction (compare dashed with solid lines). In the first hours after onset, this group shows the highest values of all experiments. The P4Kls60 experiment reaches a peak of 27%. However, the precipitation rate shows no significant difference when compared to the TEMP. Thus, we find that a modification of the large-scale convergence predominantly alters the area fraction of precipitation and not its intensity. This is in accordance with Loriaux et al. (2017) who further hypothesize that an increased large-scale vertical lifting triggers convection easier at more locations in the domain, leading to a higher area fraction but not necessarily higher precipitation rates per event.

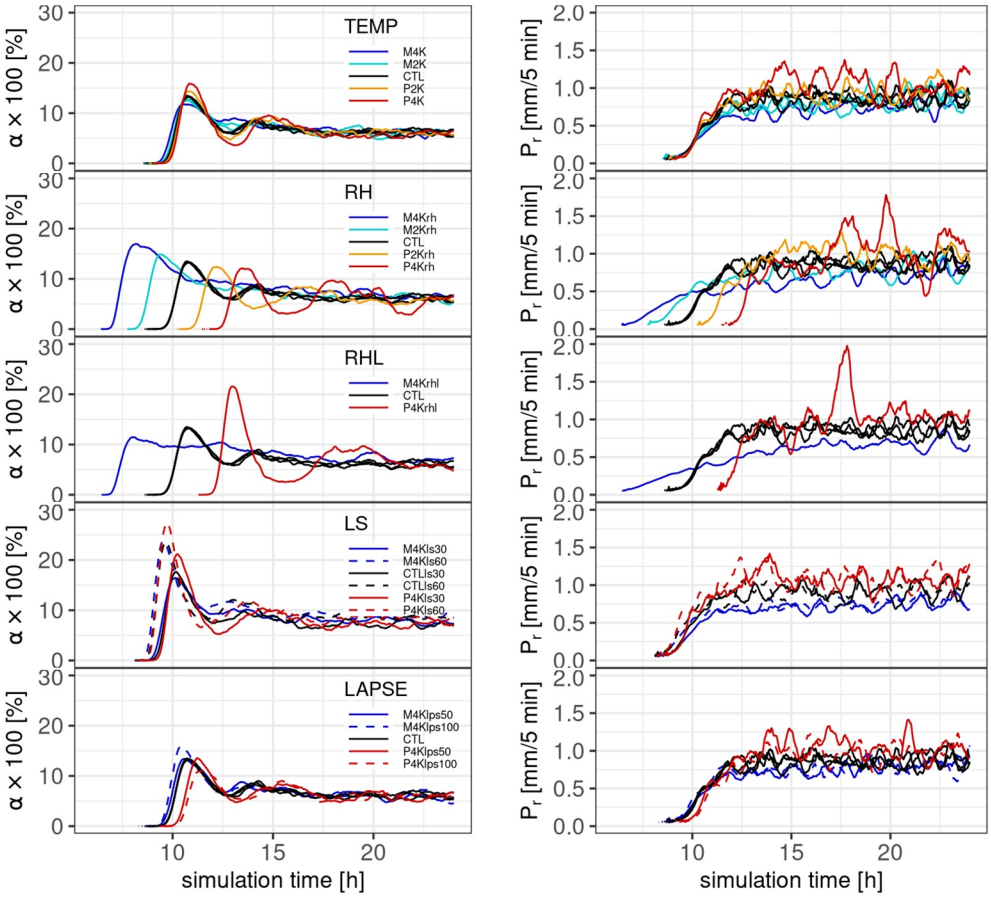

Figure 3. Time series of precipitation area fraction α (left panels) and conditional precipitation rate P_r (right panels). Each panel, from top to bottom, shows one specific perturbation group together with the control simulation.

A modification of the lapse rate has a small impact on the timing of precipitation onset. As expected, more stable conditions (in terms of lapse rate) slightly delay the onset and first peak of precipitation (as in P4Klps50 and P4Klps100), whereas the more unstable condition in the colder runs lead to slightly earlier onset of precipitation. In the most extreme experiments (P4Klps100 and M4Klps100), we find a reduced/increased precipitation area fraction in the first few hours after onset. The remaining part of the simulation in the LAPSE group shows no significant difference of area fraction between the experiments. Apart from this the precipitation rate increases from the coldest to the warmest experiments.

While domain averaged rain statistics reveal some basic properties of the response of the different experiments, they do not reveal the rain cell properties very well. In order to investigate rain cell properties in the next sections, and how they relate to the cold pool properties, we pooled data over a sufficiently long-time window of the simulation. As found in Lochbihler et al. (2019), in the course of the simulation, the precipitation field undergoes significant changes from many small cells to fewer but bigger events. Since we are particularly interested in the characteristics of convective precipitation in a more organized state, we choose to sample only events from a time window at a later stage of the simulations. Due to the obvious timing differences, we set the sampling interval relative to the time of precipitation onset. More specifically we use only data between 3 h after onset until 9 h after onset. This way we avoid a pollution of the statistics with data from around the first peak of precipitation area fraction where almost all rainfall events are of type small single-cell convection. Furthermore, the 6 h length of the time window guarantees a sufficient amount of precipitation events even for the RH and RHL groups. This choice proves robust even when choosing a different start for the analysis time window (compare Figure 5d and Figure S5).

3.2. Intensity and Size of Rain Cells

Figure 4 shows the empirical cumulative distribution function (ECDF) of cell size and intensity for the experiments in the TEMP group derived from the 6 h time window. It illustrates that the size of large rain cells (>95th percentile) increases with temperature from the M4K to the P4K experiment. Below the 95th percentile threshold, cells are smaller in colder runs compared to warmer experiments. The same observation can be made for the intensity of rain cells (Figure 4b).

Since we are particularly interested in the most extreme and largest events, and at the same time, aim at comparing all experiments in all groups, we chose to calculate a high percentile from the distributions of cell size and intensity and use this percentile in further analysis. For this purpose, we choose the 99.5th percentile which is beyond the pivot point (95th percentile) but not yet prone to be polluted by outliers and therefore poor statistics. The 99.5th percentile is marked by a black vertical line in Figures 4a and 4b. Despite the fact that other percentiles deliver very similar results (see Figure S5), we find that this choice provides the best compromise with respect to the varying sample sizes between the different experiments.

Figure 5 shows the results of this analysis. Since at first sight the results of all experimental groups may be overwhelming, we introduce this plot by separating out the results of the different experiment groups here. Figure 5a compares the TEMP and LS groups. With focus on the x-axis, it becomes clear that for both groups one can observe an increase of rain cell intensity from the coldest to the warmest experiments. Concurrently, rain cells grow in size. However, the enhanced large-scale convergence in the LS group seems to generally only increase the rain cell size while cell intensities remain virtually the same as in the TEMP group. This appears as a vertical shift, as indicated by the arrows in Figure 5a. In essence, this resembles the domain wide increase of precipitation area fraction as described in the previous section, see also Figure 3. We note that these results contradict the theory that the higher area fraction is caused by a larger number of events of roughly the same size, as speculated by (Loriaux et al., 2017).

The response to stability changes in the LAPSE group with respect to the standard group, TEMP, is less univocal (Figure 5b). While the full adiabatic perturbations, M4Klps100 and P4Klps100, are on a clear trajectory toward the CTL setup (see arrows in Figure 5b), the intermediate experiments, M4Klps50 and P4Klps50, have a less unique direction. Nonetheless, in the first case, it can be concluded that cell intensity and size are eventually both affected by this perturbation setup.

In case of the perturbations of the relative humidity, the RH and RHL groups, there are multiple aspects (Figure 5c). First, although there is no increase of rain cell intensity from the P4K to the P4Krh experiments, the rain cells are larger in the latter case (red vertical arrow). This is particularly interesting since these experiments have the same amount of water vapor in their initial profiles and differ only in temperature and thus relative humidity (see Figure S4). The opposite behavior can be observed in the case of the M4K and M4Krh experiments: cell intensity decreases while the size remains nearly the same (blue horizontal arrow). In between, the P2Krh experiment shows a different behavior. Compared to their equivalents from the TEMP group cell size and intensity increases. Even more, both cell size and intensity increase to a point that are almost equal to the ones in the P4K experiment. This means, that a slightly lower relative humidity can boost precipitation intensity and event size to an equivalent level as in a considerably moister and warmer situation. The opposite behavior can be observed for the M2K and M2Krh experiments. The diagonal arrows in Figure 5c illustrate the described shifts. The response of cell intensity and size in the RHL group seems to follow a similar path although the signal is stronger for the colder runs than for the warmer experiments. We note that enhanced warming only near the surface also changes the atmospheric stability compared to the RH group where warming is applied to the whole atmospheric column (compare CAPE time series in Figure S3). This complicates interpretation. Also, we cannot identify a reason for the upper and lower bounds on $P_{i,r}$ and L_i. We conclude that changes in relative humidity have quite strong impacts on cell size and intensity. Surprisingly, a lower relative humidity with warming leads to bigger/more intense cells, and vica versa.

In the proceeding, we will relate the rain cell properties to cold pool properties. To do so, we will take the product of rain cell area and intensity, and call this measure the cell-aggregated rain rate P_{car}, which is the total amount of rain per unit time. From the previous results it is already clear that rain cell intensity and size are well related, but it is not so clear whether the product of the 99.5th percentiles of intensity and area gives a good measure of the 99.5 percentile of cell-aggregated rain rate. Therefore, Figure 6 shows the product of

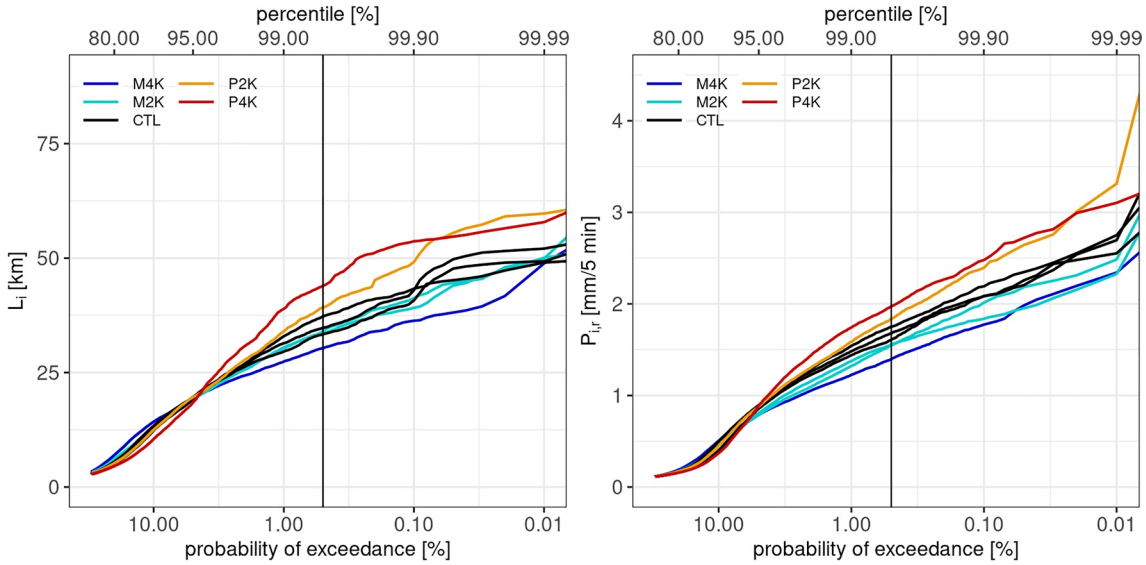

Figure 4. Probability of exceedance for rain cell size L_i (a) and average intensity $P_{i,r}$ (b) for the experiments of the TEMP group. Top axis shows corresponding percentiles. The 99.5th percentile is marked by a black vertical line.

the 99.5th percentile of cell area and average intensity (pseudo P_{car}) in relation to the true value of the 99.5th percentile of P_{car}. Despite a slight deviation from the diagonal, both quantities linearly increase from the coldest to the warmest experiments. This shows that the separate contributions of cell size and intensity to P_{car} systematically add up across all simulations. This is even closer to unity at lower percentiles (see Figure S6).

Using P_{car} as the rainfall statistics, we investigate its relation with the cold pool properties. This will be done in two separate parts. First, we concentrate on how rainfall affects cold pool dynamics. In the second part, we investigate how cold pool dynamics alter the variability of the low-level moisture field and how this could feed back to the rainfall statistics. We note that obviously these two are intertwined forming a feedback loop, yet for means of simplicity and physical understanding we present both parts separately.

3.3. Cold Pool Activity in Response to Rain Activity

We make use of two quantities related to cold pool activity. While cold pool volume measures the combined effect of the area and depth of cold pools, the growth rate indicates the speed at which active cold pools spread. Again, a percentile from the distribution of the cold pool property (growth and volume) is chosen similar to rain cell precipitation. Here, we chose the 95th percentile, which is lower than the 99.5th percentile for rain cell statistics. Since precipitation precedes the formation of a cold pool and cold pools without an associated rain cell are excluded from our analysis, sample sizes are even smaller than those for rain cells. Only selecting cold pools with increasing size, as we do in the case of cold pool growth rate, further shrinks sample sizes. Under these circumstances, we chose the 95th percentile. Testing has shown that the 95th percentile captures the most extreme cold pools in all experiment groups while still guaranteeing a robust estimate despite the varying sample sizes.

Since evaporation of rain is the primary driver for cold pools, we start by looking at the relation between the rain produced by a cell ($P_{i,car}$) and cold pool growth rate ($C_{i,gr}$), see Figure 7a. Assuming that the evaporation is proportional to the rain cell rain rate, we expect a good correlation. Indeed, a very strong relation is found between $P_{i,car}$ and cold pool growth rate, with data almost on a straight line (through the origin). In general, larger and stronger precipitating rain cells cause faster spreading cold pools. However, the strength of the response depends on the initial temperature. $C_{i,gr}$ and $P_{i,car}$ rather weakly increase with initial temperature in the coldest simulations. Those experiments are densely packed in the lower left corner of Figure 7a. In warmer simulations, we find that the spread increases the higher the temperature.

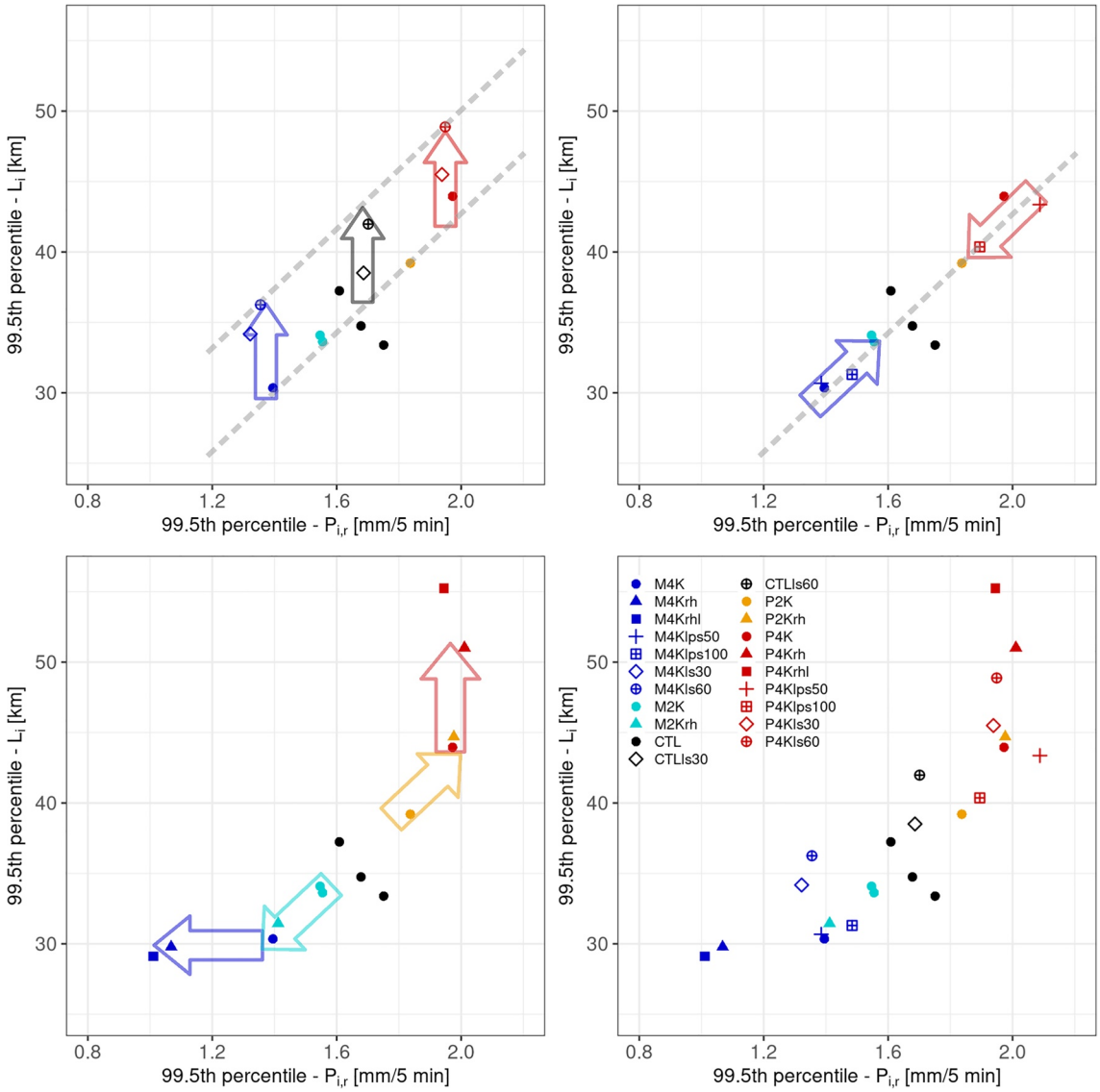

Figure 5. The 99.5th percentile of cell average intensity $P_{i,r}$ versus rain cell size L_i. Panel (a) shows the TEMP and LS groups, (b) the TEMP and LAPSE groups, (c) the TEMP, RH, and RHL groups. All groups together are depicted in (d). Arrows illustrate relative changes with respect to the TEMP group (see text).

Looking specifically at the TEMP group, we find that cold pool growth rate continuously and strongly increases with higher temperature and moisture availability from the M4K to the P4K experiment. The stronger large-scale convergence in the LS group virtually has no additional effect on the cold pool growth rate when compared to the TEMP group despite the presence of larger rain cells (see Figure 5a). In the LAPSE group, the previously described trajectory from the corresponding experiments in the TEMP group toward the CTL run appears to be a persistent feature: Cold pool growth rate decreases along with rain cell-aggregated rain rate from the P4K to the P4Klps100 experiment and vice versa from M4K to M4Klps100. The RH and RHL however respond differently in terms of the cold pool volume. The experiments in both groups show, in relation to their partners in the TEMP group, a further amplification of the signal. For instance, $C_{i,gr}$ further increases from the P2K to the P2Krh and from the P4K to the P4Krh experiments. The P4Krhl experiment has the fastest spreading cold pools. Cold pool growth rate in the M2Krh, M4Krh and M4Krhl experiments responds the opposite way, although the signal is rather weak in this case. We therefore conclude that evaporation of precipitation, the main driver of cold pools, further increases at decreased relative humidity and, thus, leading to stronger cold pools at comparable rainfall intensity in an atmosphere which is closer to saturation (e.g., compare P4K and P4Krh experiments).

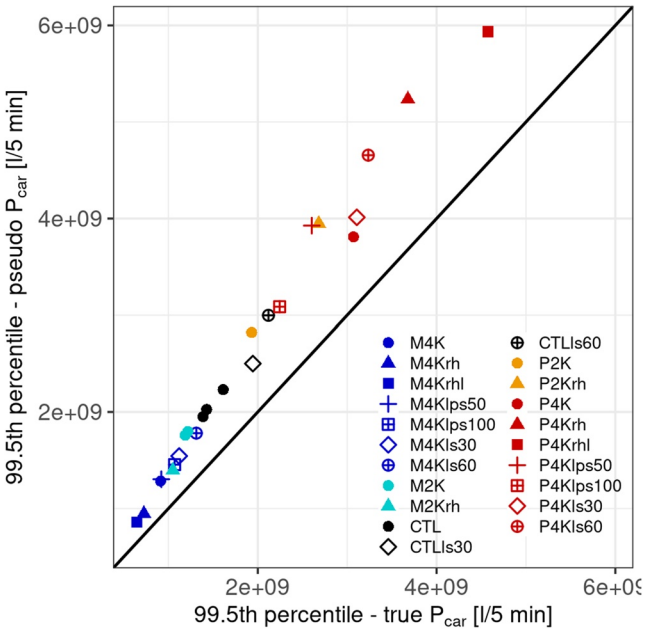

Figure 6. A comparison of the product of the 99.5th percentiles of cell intensity and area (pseudo P_{car}) and the true value of the cell-aggregated rain rate (true P_{car}).

Due to the nature of cold pools which are essentially density currents, one would expect that faster spreading cold pools are associated with a stronger and more spacious θ_e anomaly. Figure 7b confirms this relation. Cold pool volume—the product of the average θ_e anomaly and the area of a cold pool—linearly increases with cold pool growth rate, and therefore with the initial temperature of the different simulations. Again, the rate of increase with initial temperature is lower for colder simulations than for the warmest. Particularly the warmest experiments in the RH and RHL groups exhibit a strong increase when compared to the TEMP group. The damping effect of a more stable atmosphere on the warmer side of the LAPSE experiments is also reflected here in form of smaller and weaker cold pools which eventually spread slower.

3.4. Low-Level Moisture and Rain Activity in Response to Cold Pool Activity

One of the key characteristics of laterally spreading cold pools is that they create a divergent wind field near the surface, and areas of convergence at the cold pool fronts and where different cold pool collide (Schlemmer & Hohenegger, 2014). Given the presence of multiple cold pools in different locations, this eventually leads to confined regions with strongly enhanced moisture content (see Figure 2).

We quantify these relatively moist regions in the domain by the product of their average moisture content and area, called moist patch volume. In analogy to previous figures, we draw a high percentile from the distribution of moist patch volume for all experiments. We chose the 95th percentile since sample sizes are relatively small compared to rain cells.

A direct comparison with cold pool volume, see Figure 8a, illustrates the effect of cold pool activity on the low-level moisture field. Warmer conditions generally lead to larger moist patches of higher moisture content. Moist patch volume is roughly four times higher in the P4K experiment than in the M4K run. The effect is, however, stronger for simulations warmer than CTL. Colder model runs are densely packed together at relatively low moist patch volumes. In particular, the relation with cold pool volume reveals that small, shallow and, thus, slowly spreading cold pools in the coldest simulations create moist patches which barely

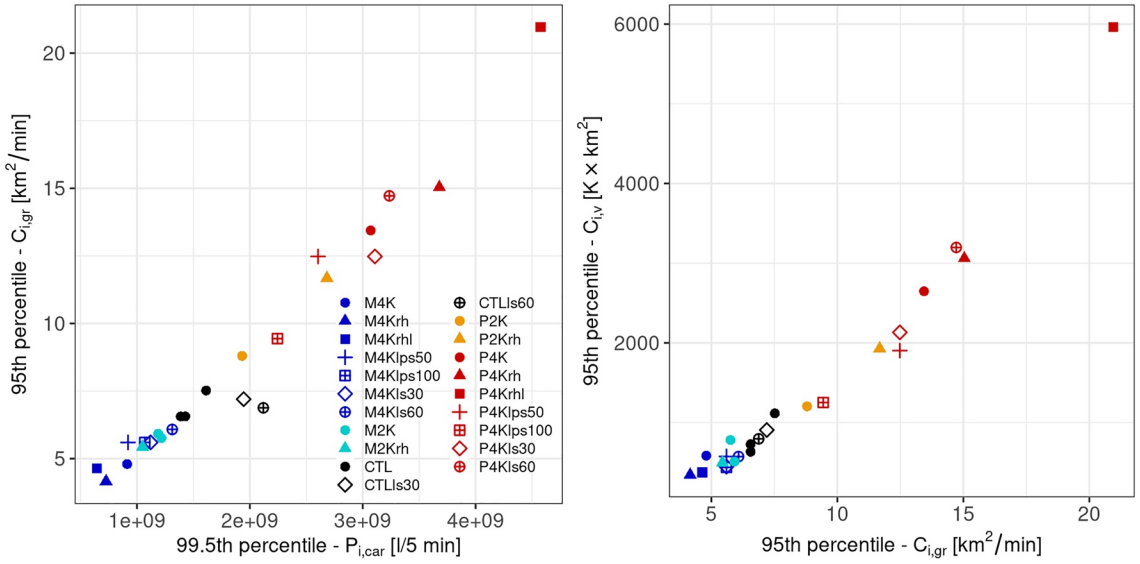

Figure 7. Cell-aggregated rain rate $P_{i,car}$ in relation to cold pool growth rate $C_{i,gr}$ (a) and cold pool growth rate compared to cold pool volume $C_{i,v}$ (b).

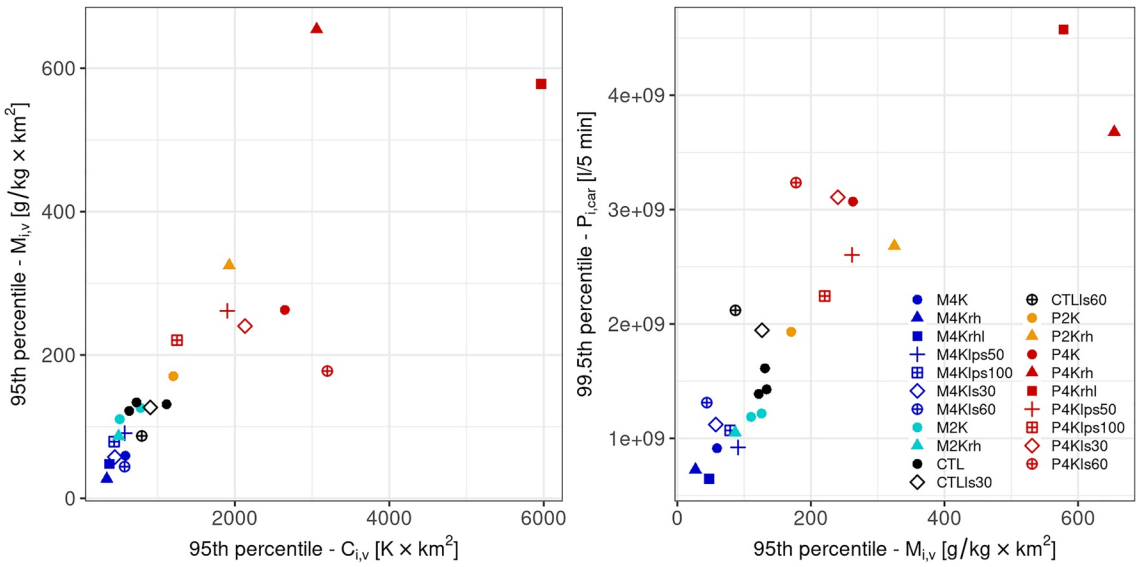

Figure 8. The 95th percentile of cold pool volume $C_{i,v}$ compared to moist patch volume $M_{i,v}$ (a) and moist patch volume compared to cell-aggregated rain rate $P_{i,car}$ (b).

emerge above the average q_v field. For instance, the M4Krh simulation stands out with very small cold pool and moist patch volumes. In contrast to that, the warmest simulations in the RH and RHL groups have, by far, the highest moist patch volume. Compared to the TEMP group, amplified cold pools due to a reduction of relative humidity boost the accumulation of moisture in confined regions. Lower precipitation amounts due to increased stability in the P4Klps100 experiment lead to weaker cold pool activity and eventually to a slightly smaller cold pool volume as in the corresponding simulation from the TEMP group (and vice versa for the M4Klps100 experiment). Interestingly, the strongly enhanced large-scale convergence in the CTLls60 and P4Kls60 experiments seems to reduce the moist patch volume. The reason for this behavior is not completely clear since there is virtually no change in cold pool activity (with respect to the TEMP group). Even more, the slightly increased cold pool volume and growth rate in the P4Kls60 experiment suggests the formation of wetter and larger moist patches. Thus, we speculate that the applied threshold for the moist patch clustering plays a role in this case. A strong uniformly applied moisture tendency through large-scale convergence causes the domain averaged specific humidity q_v to increase. This average is mostly dependent on grid points outside moist patches (see Figure 2). A threshold of 0.75 g kg^{-1} might then be too high which potentially leads to relatively smaller moist patches after the clustering with eventually lower moist patch volume.

To examine how a concentrated accumulation of moisture through cold pools feeds back to precipitation amounts Figure 8b depicts the relation between moist patch volume and cell-aggregated rain rate. We find that increased moist patch volume at higher temperatures correlates well with enhanced rain cell intensity and size. The previously described tendencies in each perturbation group hold well in this context. For instance, the experiments in the TEMP group reveal a strongly linear correlation between moist patch volume and cell-aggregated rain rate. When compared to the RH and RHL groups, reduced relative humidity leads to higher precipitation amounts inside rain cells (and vice versa). The LAPSE group confirms that when the temperature perturbation approaches a moist adiabat, and therefore stabilizes the atmosphere, attenuates the signal in comparison with the TEMP group. In the case of the LS group, despite increased cell-aggregated rain rates, we find no further increase in moist patch volume when compared to the TEMP group.

As a final remark, we note that, despite there is a clear relation between cold pool activity, moist patch volume, and rain event intensity, the described processes are intertwined and progress concurrently, possibly at different stages. This limits the ability to derive a direct causality from the presented statistics alone. However, it has been shown that new deep convective clouds form at locations of elevated moisture, of which a substantial part stems from the advection through cold pools (Schlemmer & Hohenegger, 2016). This link is further strengthened in a more recent study by Fuglestvedt and Haerter (2020). They use a backtracking approach to

identify cold pools as moisture conveyors for newly emerging deep convective clouds. In a more qualitative way, this process can be observed in video animation V1 where "waves" of warm and moist low-level air masses with high θ_e at the cold pool fronts "disappear" at locations where new rain cells appear slightly later.

4. Conclusion

In this study, we examined the impact of various atmospheric perturbations, which are relevant in the context of climate change, on the characteristics of rain in convective cloud systems. To this end, we created a set of high-resolution large eddy simulations for a typical convective event at midlatitudes over a range of dew point temperatures, and in addition, groups based on accompanying changes in relative humidity, temperature lapse rate, and large-scale convergence. With this set of experiments aimed to represent different climatic conditions, we examined how, and to which extent, cold pools relate to rain cell size and intensity.

A general conclusion for all experimental groups is a general increase of intensity and size of precipitation events with higher temperatures. The warmest simulations show the strongest signal. However, the details of the response in each experimental group differ. For instance, we find that enhanced large-scale convergence under warmer conditions (LS group) only increases event size when compared to the latter alone (TEMP group). A stabilization of the atmosphere under warmer conditions according to a moist adiabat (LAPSE group) hampers the development of intense rain events under warmer conditions and, thus, weakens the signal when compared to a vertically uniform warming (TEMP group). Finally, a modification of the relative humidity with warming (RH and RHL groups) bears the strongest response of intensity and size of rainfall events. However, this comes at the cost of number of events due to a later onset of precipitation in the course of the simulations. In other words, rain events become more rare but their extremes increase at a much higher rate when compared to a constant relative humidity perturbation (TEMP group).

Cold pool activity concurrently increases with stronger and larger rainfall events under warmer conditions, confirming results in Haerter and Schlemmer (2018). A very strong relation between the aggregated rain rate of extreme cells and the growth rate and size of cold pools is found, unifying all experiments onto an almost single curve relating rain rate to the cold pool statistics. In this case, the warmer runs with decreased relative humidity lead to the largest cold pools. Thus, we can identify two fundamental factors in our simulations that control the magnitude of cold pool activity. First, higher precipitation rates enable more evaporation of rain drops. This enhances the cooling rate of air masses which eventually form the cold pool. Second, a reduced relative humidity causes enhanced evaporation of rain drops at similar precipitation rates. The combined effect of these processes causes the warmer experiments with lower relative humidity to have the strongest response in cold pool dynamics.

Reversely, cold pool dynamics appear to influence local low-level moisture variability and subsequent rainfall formation, affirming Schlemmer and Hohenegger (2016), but now in a climate change context. Although the relation between cold pool statistics and moist patches—amount of excess moisture contained in confined, moist areas—appears less distinct, larger cold pools generally lead to larger moist patches. Subsequently, larger moist patches again translate into larger aggregated rain rates from rain cells. Physically, enhanced cold pool activity amplifies the advection of moisture into confined regions and this directly relates to intensified rainfall events. The most intense and fastest spreading cold pools are found in the warmest simulations. This enables moisture transport over longer distances and greater accumulation into moist patches. Again the warmest, lower relative humidity runs lead to the largest moist patches.

Concluding, we showed that cold pools play a crucial role in shaping the response of convective rain extremes in a large set of simulations, representing different climatic conditions. In general, cold pool dynamics increase in warmer conditions, and we speculate that this feedback loop might play an important role explaining deviations from the CC-scaling in the response of rain extremes to global warming. Yet, we also note that the stabilization of the atmosphere (according to a moist adiabatic lapse rate) appears to dampen feedback from cold pools dynamics but on the other hand projected decreases in relative humidity appear to strongly amplify their influence. Further investigating these feedback processes, preferably also in different modeling setups, is therefore highly recommended.

Data Availability Statement

A data set with the DALES case setup is available from https://doi.org/10.4121/13241072, the video animation from https://doi.org/10.4121/13241081, and the software used for clustering can be found under https://doi.org/10.4121/13241102.

Acknowledgments
The authors are grateful for the funding from the Netherlands Organisation for Scientific Research (NWO), project Space2rain (869.15.002). Simulations were carried out at the ECMWF computing facilities within the special project SPACELES. Lenderink acknowledges financial support from the project INTENSE, which is supported by the European Research Council (grant: ERC-2013-CoG, project 617329). Lochbihler thanks Jan Haerter for many inspiring discussions during a 1-month sabbatical in his research group at the Niels Bohr Institute, University of Copenhagen.

References

Attema, J., Loriaux, J., & Lenderink, G. (2014). Extreme precipitation response to climate perturbations in an atmospheric mesoscale model. *Environmental Research Letters*, *9*(1), 014003. https://doi.org/10.1088/1748-9326/9/1/014003

Berg, P., Moseley, C., & Haerter, J. O. (2013). Strong increase in convective precipitation in response to higher temperatures. *Nature Geoscience*, *6*, 181. https://doi.org/10.1038/ngeo1731

Böing, S. J., Jonker, H. J. J., Siebesma, A. P., & Grabowski, W. W. (2012). Influence of the subcloud layer on the development of a deep convective ensemble. *Journal of the Atmospheric Sciences*, *69*(9), 2682–2698. https://doi.org/10.1175/JAS-D-11-0317.1

Bony, S., Colman, R., Kattsov, V. M., Allan, R. P., Bretherton, C. S., Dufresne, J.-L., et al. (2006). How well do we understand and evaluate climate change feedback processes? *Journal of Climate*, *19*(15), 3445–3482. https://doi.org/10.1175/JCLI3819.1

Fildier, B., Parishani, H., & Collins, W. D. (2017). Simultaneous characterization of mesoscale and convective-scale tropical rainfall extremes and their dynamical and thermodynamic modes of change. *Journal of Advances in Modeling Earth Systems*, *9*(5), 2103–2119. https://doi.org/10.1002/2017MS001033

Fuglestvedt, H. F., & Haerter, J. O. (2020). Cold pools as conveyor belts of moisture. *Geophysical Research Letters*, *47*(12), e2020GL087319. https://doi.org/10.1029/2020GL087319

Grabowski, W. W. (1998). Toward cloud resolving modeling of large-scale tropical circulations: A simple cloud microphysics parameterization. *Journal of the Atmospheric Sciences*, *55*(21), 3283–3298. https://doi.org/10.1175/1520-0469(1998)055⟨3283:TCRMOL⟩2.0.CO;2

Haerter, J. O., Böing, S. J., Henneberg, O., & Nissen, S. B. (2019). Circling in on convective organization. *Geophysical Research Letters*, *46*(12), 7024–7034. https://doi.org/10.1029/2019GL082092

Haerter, J. O., & Schlemmer, L. (2018). Intensified cold pool dynamics under stronger surface heating. *Geophysical Research Letters*, *45*(12), 6299–6310. https://doi.org/10.1029/2017GL076874

Heus, T., van Heerwaarden, C. C., Jonker, H. J. J., Pier Siebesma, A., Axelsen, S., van den Dries, K., et al. (2010). Formulation of the dutch atmospheric large-eddy simulation (dales) and overview of its applications. *Geoscientific Model Development*, *3*(2), 415–444. https://doi.org/10.5194/gmd-3-415-2010

Hirt, M., Craig, G. C., Schäfer, S. A. K., Savre, J., & Heinze, R. (2020). Cold-pool-driven convective initiation: Using causal graph analysis to determine what convection-permitting models are missing. *Quarterly Journal of the Royal Meteorological Society*, *146*(730), 2205–2227. https://doi.org/10.1002/qj.3788

Khairoutdinov, M., & Randall, D. (2006). High-resolution simulation of shallow-to-deep convection transition over land. *Journal of the Atmospheric Sciences*, *63*(12), 3421–3436. https://doi.org/10.1175/JAS3810.1

Lenderink, G., Barbero, R., Loriaux, J. M., & Fowler, H. J. (2017). Super-Clausius-Clapeyron scaling of extreme hourly convective precipitation and its relation to large-scale atmospheric conditions. *Journal of Climate*, *30*(15), 6037–6052. https://doi.org/10.1175/JCLI-D-16-0808.1

Lenderink, G., Mok, H. Y., Lee, T. C., & Van Oldenborgh, G. J. (2011). Scaling and trends of hourly precipitation extremes in two different climate zones—Hong Kong and the Netherlands. *Hydrology and Earth System Sciences*, *15*(9), 3033–3041. https://doi.org/10.5194/hessd-8-4701-2011

Lenderink, G., & van Meijgaard, E. (2008). Increase in hourly precipitation extremes beyond expectations from temperature changes. *Nature Geoscience*, *1*(8), 511–514. https://doi.org/10.1038/ngeo262

Lochbihler, K., Lenderink, G., & Siebesma, A. P. (2017). The spatial extent of rainfall events and its relation to precipitation scaling. *Geophysical Research Letters*, *44*(16), 8629–8636. https://doi.org/10.1002/2017GL074857

Lochbihler, K., Lenderink, G., & Siebesma, A. P. (2019). Response of extreme precipitating cell structures to atmospheric warming. *Journal of Geophysical Research: Atmospheres*, *124*(13), 6904–6918. https://doi.org/10.1029/2018JD029954

Loriaux, J. M., Lenderink, G., Roode, S. R. D., & Siebesma, A. P. (2013). Understanding convective extreme precipitation scaling using observations and an entraining plume model. *Journal of the Atmospheric Sciences*, *70*(11), 3641–3655. https://doi.org/10.1175/JAS-D-12-0317.1

Loriaux, J. M., Lenderink, G., & Siebesma, A. P. (2017). Large-scale controls on extreme precipitation. *Journal of Climate*, *30*(3), 955–968. https://doi.org/10.1175/JCLI-D-16-0381.1

Moseley, C., Berg, P., & Haerter, J. O. (2013). Probing the precipitation life cycle by iterative rain cell tracking. *Journal of Geophysical Research: Atmospheres*, *118*(24), 13361–13370. https://doi.org/10.1002/2013JD020868

O'Gorman, P. A., & Muller, C. J. (2010). How closely do changes in surface and column water vapor follow clausius–clapeyron scaling in climate change simulations? *Environmental Research Letters*, *5*(2), 025207. https://doi.org/10.1088/1748-9326/5/2/025207

Pall, P., Allen, M. R., & Stone, D. A. (2007). Testing the Clausius–Clapeyron constraint on changes in extreme precipitation under CO_2 warming. *Climate Dynamics*, *28*(4), 351–363. https://doi.org/10.1007/s00382-006-0180-2

Romps, D. M. (2011). Response of tropical precipitation to global warming. *Journal of the Atmospheric Sciences*, *68*(1), 123–138. https://doi.org/10.1175/2010JAS3542.1

Schlemmer, L., & Hohenegger, C. (2014). The formation of wider and deeper clouds as a result of cold-pool dynamics. *Journal of the Atmospheric Sciences*, *71*(8), 2842–2858. https://doi.org/10.1175/JAS-D-13-0170.1

Schlemmer, L., & Hohenegger, C. (2016). Modifications of the atmospheric moisture field as a result of cold-pool dynamics. *Quarterly Journal of the Royal Meteorological Society*, *142*(694), 30–42. https://doi.org/10.1002/qj.2625

Seifert, A., & Heus, T. (2013). Large-eddy simulation of organized precipitating trade wind cumulus clouds. *Atmospheric Chemistry and Physics*, *13*(11), 5631–5645. https://doi.org/10.5194/acp-13-5631-2013

Tebaldi, C., Hayhoe, K., Arblaster, J. M., & Meehl, G. A. (2006). Going to the extremes. *Climatic Change*, *79*(3), 185–211. https://doi.org/10.1007/s10584-006-9051-4

Tett, S. F. B., Mitchell, J. F. B., Parker, D. E., & Allen, M. R. (1996). Human influence on the atmospheric vertical temperature structure: Detection and observations. *Science*, *274*(5290), 1170–1173. https://doi.org/10.1126/science.274.5290.1170

Tompkins, A. M. (2001). Organization of tropical convection in low vertical wind shears: The role of cold pools. *Journal of the Atmospheric Sciences*, *58*(13), 1650–1672. https://doi.org/10.1175/1520-0469(2001)058⟨1650:OOTCIL⟩2.0.CO;2

Torri, G., Kuang, Z., & Tian, Y. (2015). Mechanisms for convection triggering by cold pools. *Geophysical Research Letters*, *42*(6), 1943–1950. https://doi.org/10.1002/2015GL063227

Trenberth, K. E., Dai, A., Rasmussen, R. M., & Parsons, D. B. (2003). The changing character of precipitation. *Bulletin of the American Meteorological Society*, *84*(9), 1205–1217. https://doi.org/10.1175/BAMS-84-9-1205

Wasko, C., Lu, W. T., & Mehrotra, R. (2018). Relationship of extreme precipitation, dry-bulb temperature, and dew point temperature across Australia. *Environmental Research Letters*, *13*(7), 074031. https://doi.org/10.1088/1748-9326/aad135